Interactions between deforestation, landscape rejuvenation, and shallow landslides in the North Tanganyika - Kivu Rift region, Africa

Arthur Depicker[1], Gerard Govers[1], Liesbet Jacobs[1], Benjamin Campforts[2], Judith Uwihirwe[3,4], and Olivier Dewitte[5]

[1]KU Leuven, Department of Earth and Environmental Sciences, Division of Geography and Tourism (Celestijnenlaan 200E, 3001 Heverlee, Belgium)
[2]CSDMS, Institute for Arctic and Alpine Research, University of Colorado at Boulder (Boulder, CO, USA)
[3]University of Rwanda, Department of Soil and Water Management, Faculty of Agricultural Engineering (Street KK 737, Kigali, Rwanda)
[4]Delft University of Technology, Faculty of Civil Engineering and Geosciences, Department of Water Management (Stevinweg 1, 2628 Delft, The Netherlands)
[5]Royal Museum for Central Africa, Department of Earth Sciences (Leuvensesteenweg 13, 3080 Tervuren, Belgium)

Correspondence: Arthur Depicker (arthur.depicker@kuleuven.be)

Abstract. Deforestation increases landslide activity over short, contemporary timescales. However, over longer timescales the location and timing of landsliding is controlled by the interaction between uplift and fluvial incision. Yet, the interaction between (human-induced) deforestation and landscape evolution has hitherto not been explicitly considered. We address this issue in the North Tanganyika-Kivu Rift region (East African Rift). In recent decades, the regional population has grown

5 exponentially and the associated expansion of cultivated and urban land has resulted in widespread deforestation. On a much longer time scale, tectonic uplift has forged two parallel mountainous Rift shoulders that are continuously rejuvenated through knickpoint retreat, enforcing topographic steepening. In order to link deforestation and rejuvenation to landslide erosion, we compiled an inventory of nearly 8,000 recent shallow landslides in © Google Earth imagery from 2000-2019. To accurately calculate landslide erosion rates, we developed a new methodology to remediate inventory biases linked to the spatial and

10 temporal inconsistency of this satellite imagery. We find that erosion rates in rejuvenated landscapes are roughly 40 % higher than in the surrounding relict landscapes, upstream of retreating knickpoints and outside of the Rift shoulders. This difference is due to the generally steeper relief in rejuvenated landscapes which more than compensates for the fact that rejuvenated slopes, when compared to similarly angled slopes in relict zones, often display a somewhat lower landslide erosion rate. These lower rates in the rejuvenated landscapes could be the result of a drier climate, the omission of earthquake-induced

15 landslide events in our landslide inventory, and potentially a smaller regolith stock. More frequent extreme rainfall events in the relict zones, and possibly the presence of a thicker regolith, cause a stronger landslide response to deforestation compared to rejuvenated landscapes. Overall, deforestation initiates a landslide peak that lasts approximately 15 years and increases landslide erosion by a factor 2 to 8. Eventually, landslide erosion in deforested land falls back to a level similar to that observed under forest conditions, most likely due to the depletion of the most unstable regolith. Landslides are not only more abundant

20 in rejuvenated landscapes but are also smaller in size, which may be a consequence of the seismic activity that fractures the

Earth Surface
Dynamics
Discussions
Open Access
EGU

bedrock and reduces the minimal critical area for slope failure. With this paper, we highlight the importance of considering the geomorphological context when studying the impact of recent land use changes on landslide activity.

1 Introduction

25   On steep terrain, shallow landslide erosion increases significantly as a result of deforestation (e.g. Montgomery et al., 2000; Mugagga et al., 2012). The removal of trees, due to either human or natural causes, decreases the slope stability through the alteration of hydrological and geotechnical conditions, such as the loss in soil cohesion due to tree root decay (Sidle et al., 2006; Sidle and Bogaard, 2016). After 10-20 years, depending on the climate and vegetation regeneration rate, this effect starts wearing off (Sidle and Bogaard, 2016). However, when forests are permanently converted to grassland or cropland, the

30   consequences of deforestation for landsliding can last much longer or even be permanent (Sidle et al., 2006).

While these general principles are now well described, we do not yet fully understand the extent to which deforestation increases landslide erosion in different types of landscapes. A key distinction can be made here between actively incising, rejuvenating landscapes, in which landslides are a prime slope-limiting mechanism and 'old', so-called relict landscapes, where hillslopes have had a long time to adapt to river incision (Burbank et al., 1996; Larsen and Montgomery, 2012). These

35   two landscape types can be expected to respond differently to deforestation: in rejuvenating landscapes hillslopes are already continuously adapting to river incision through landsliding (Egholm et al., 2013). In relict landscapes, on the other hand, hillslopes will slowly become less steep and landslides occur more sporadically, potentially allowing for a thick regolith cover to develop (Schoenbohm et al., 2004; Bennett et al., 2016). Climatic variations can also drive differences in landscape response to deforestation (Crozier, 2010), and in the context of lithologically diverse landscapes, the effect of rock strength on both

40   knickpoint retreat and landsliding must also be acknowledged (Parker et al., 2016; Baynes et al., 2018; Campforts et al., 2020).

Here, we aim to explore the interplay of deforestation and uplift-driven landscape rejuvenation on shallow landslide erosion. We focus our research on the North Tanganyika-Kivu Rift region (hereafter referred to as 'the NTK Rift', **Fig. 1**), part of the western branch of the East African Rift. Deforestation, mainly driven by agriculture, is widespread and a result of the fast-growing population (from 89 inhabitants per km^2 in 1975 to 241 inhabitants per km^2 in 2015) (Hansen et al., 2013; JRC and

45   CIESIN, 2015; Musumba Teso et al., 2019). Furthermore, the area is characterized by frequent landsliding, mostly triggered by rainfall (Monsieurs et al., 2018a; Depicker et al., 2020; Dewitte et al., 2020).

Active continental rifting in our study area is driven by the divergence of the Victoria and Nubia plates that started 11 Ma ago and currently continues at a rate of ca. 2 mm/yr (Saria et al., 2014). Due to this setting, there is widespread seismic activity, active volcanism, and uplift initiating landscape rejuvenation through knickpoint retreat (Smets et al., 2015; Delvaux et al.,

50   2017; Dewitte et al., 2020). Adding to the geological complexity of the NTK Rift is the wide variability in age and strength of rock formations. The majority of rocks in the northern and eastern parts of the study area are of Mesoproterozoic age (1600-720
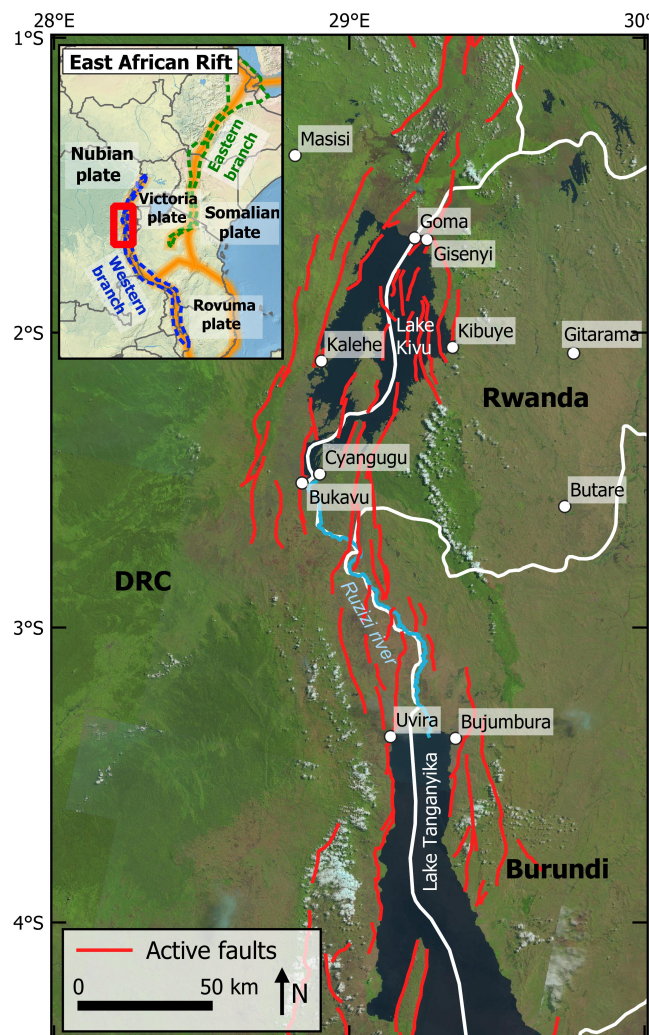
Figure 1. Overview of the NTK Rift and its active faults (Delvaux and Barth, 2010). LANDSAT-8 imagery is used as background (USGS, 2018).

Ma), being mostly quartzites, granites, or pelites. The southwest is largely cover ed by either weathering-resistant quartzites or weathering-prone gneiss and micaschists of Paleoproterozoic age (2500-1600 Ma). Within the Rift shoulders, the same pattern of Meso- and Paleoproterozoic rocks is observed, save for the occurrence of much younger lithologies such as the river and

55   lake sediments in the Ruzizi floodplain and the volcanic deposits (12 Ma - present) found around Bukavu and north of Goma (Delvaux et al., 2017; Laghmouch et al., 2018).

Until recently, the entire study area was covered in forests. Only since the beginning of the 20th century, has large scale deforestation taken place, especially between the Rift shoulders and in Rwanda and Burundi (Ellis et al., 2010; Aleman et al.,
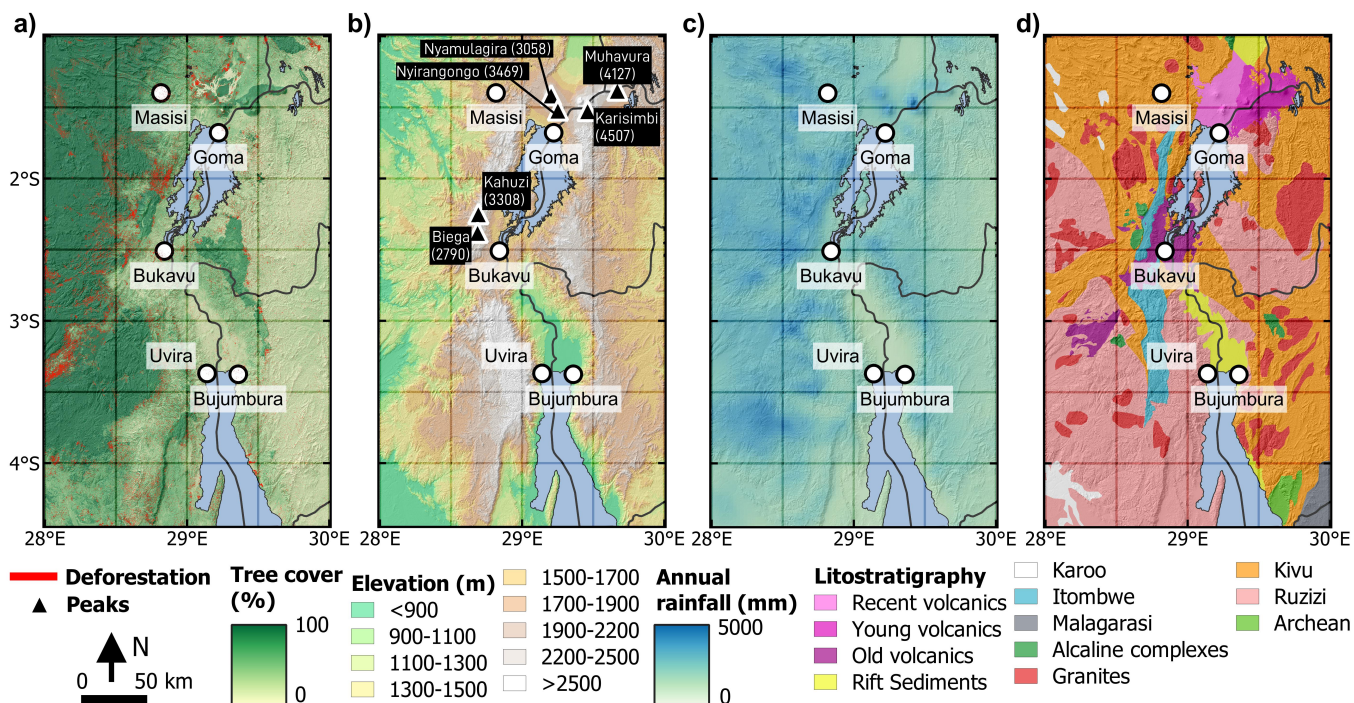
Figure 2. Environmental characterization of the NTK Rift. a) Tree cover for the year 2000 and deforestation from 2001-2017 (Hansen et al., 2013). **b)** Elevation and mountain peaks (USGS, 2006). **c)** Average annual rainfall between 2005-2015 (Van de Walle et al., 2019). d) Lithostratigraphy (**Table 1**) (Laghmouch et al., 2018).

2018). In 2000, the study area (ca. 88,500 km^2) had an estimated forest coverage of 73.1 %. Between 2001 and 2018, 4.5 % of these forests were cleared, mainly for the purpose of agriculture (Hansen et al., 2013; Tyukavina et al., 2018; Musumba Teso et al., 2019). The study area is therefore an ideal setting to evaluate how deforestation affects landslide erosion in different landscape settings.

2   Methods

In the sections below, we first focus on the landscape characteristics of the NTK Rift that can exert a control on landslide erosion: forests, rejuvenation, rainfall, and rock strength. Next, we elaborate on the different aspects of the landslide erosion assessment: the compilation of an inventory and the calculation of shallow landslide erosion rates (whether or not in the context of the previously determined landscape characteristics).
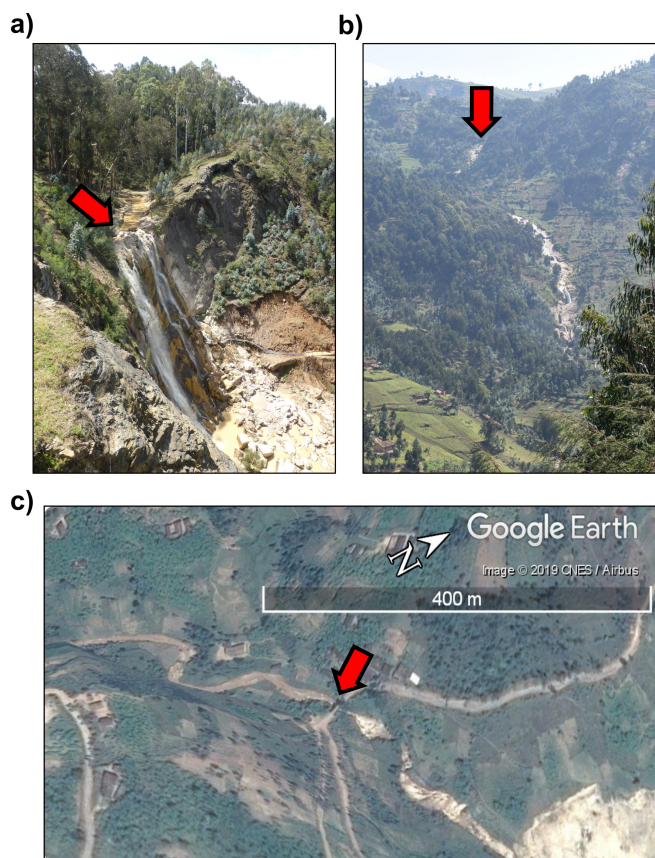
Figure 3. Field-validated knickpoints in Rwanda. The red arrow indicates the location of the knickpoint. **a)** East of Mabanze, Rwanda (29.469678° E, 2.047852° S). **b)** East of Kanama, Rwanda (29.391763° E, 1.705683° S). **c)** Southwest of Kibilira, Rwanda (29.61586° E, 1.980443° S; image ©2019 Google Earth).

2.1 Regional controls on landslide erosion

2.1.1 Forest cover and deforestation

70 We characterize the NTK Rift in terms of forest dynamics by means of the global forest data presented by (Hansen et al., 2013, *updated in 2018*) (**Fig. 2a**). This dataset contains a tree cover map for the year 2000 and forest loss data for the period 2001-2017, both provided at a resolution of one arc-second (ca. 30 m). The tree cover data shows the percentage of tree coverage in 2000 and the forest loss data displays discrete values between 1 and 17, indicating the year in which deforestation took place. Based on these data, we distinguish three land cover classes: i) forest, having >25 % tree cover (as suggested by

75 Hansen et al. (2013)), ii) deforested land, and iii) non-forest land, with ≤25 % tree cover. Both deforested and non-forest land encompass land use classes such as bare land, cropland, grassland, and urban land. There is no difference between 'non-forest'

and 'deforested' land, except for the elapsed time since deforestation. 'Non-forest' land has suffered deforestation before the year 2000, while 'deforested' land experienced deforestation over the last two decades.

2.1.2   Landscape rejuvenation

80   To delineate the rejuvenated and relict landscapes, we use the spatial pattern of knickpoints migrating upstream towards the Rift shoulders, away from the active faults. Anchored knickpoints, here defined at a distance shorter than 1 km from a geological contact, are considered unrelated to the rejuvenation process and removed from the analysis (Kirby and Whipple, 2012; Bennett et al., 2016; Schwanghart and Scherler, 2017). Two criteria are applied to identify the rejuvenated Rift: (i) the area must drain towards Lake Kivu or Lake Tanganyika, and (ii) the area must be located downstream of any knickpoint, unless there is no

85   knickpoint observed in the area. In the latter case, we assume the knickpoint reached the Rift shoulder and the landscape is completely rejuvenated.

We use the KNICKPOINTFINDER function in TopoToolbox to identify knickpoints. This function requires a drainage network and tolerance value, reflecting the maximum expected error in the true river profiles (Schwanghart and Scherler, 2017). The drainage network for this purpose is modeled with the 1 arc second SRTM DEM data (USGS, 2006) and a threshold catchment

90   area of $2{\times}10^6$ m^2. The tolerance value is used to distinguish knickpoints from discrepancies in the longitudinal river profile that are caused by errors in the DEM data. The tolerance value is calculated as the maximal difference between the 90th and 10th quantile of the smoothed river profiles (Schwanghart and Scherler, 2017), and subsequently lowered until the algorithm identifies the three knickpoints we validated in the field (**Fig. 3**).

2.1.3   Rainfall

95   Active rifting does not only trigger landscape rejuvenation but also impacts local rainfall patterns (Van de Walle et al., 2019). The majority of observed recent shallow landslides in the NTK Rift are rainfall-triggered (Monsieurs et al., 2018a; Depicker et al., 2020; Dewitte et al., 2020). To explore any relationship between rejuvenation and rainfall, we analyze two metrics: the average annual rainfall and the number of times where accumulated rainfall was sufficiently large to trigger landsliding. Based on the landslide initiation model of Guzzetti et al. (2008), we assume this criterion is met when there is more than 15 mm

100   rainfall over a period of two days. For the comparison of rainfall patterns between rejuvenated and relict landscapes, we apply the non-parametric Mann-Whitney U test, whereby each observation is the average metric (rainfall or threshold exceedance) in fifth order catchments. These units are derived from the 30 m DEM using a river catchment threshold of 10^5 m^2. The rainfall pattern is derived from the COSMO-CLM regional climate model proposed by Van de Walle et al. (2019) which has a spatial resolution of 2.8 km and a temporal resolution of 1 hour (**Fig. 2c**). Note that the spatial resolution of the rainfall products might

105   be too low to fully capture the impact of orographic controls and the local convective storm patterns (Monsieurs et al., 2018b).

Earth **Surface**
Dynamics
Discussions

Age	Chronostratigraphy	Lithostratigraphy	Main lithological constitution
10 Ka - present	Late Quaternary	Recent volcanics	lava, tuff, and ash, deposited in the past decades and centuries, a result of eruptions of the Nyiragongo and Nyamulagira.
2–1 Ma	Early Quaternary	Young volcanics	Relatively fresh basalts, deposited ± 2 Ma ago.
12–6 Ma	Neogene	Old volcanics	Highly weathered basalt, deposited 11-4 Ma years ago.
23 Ma - present	Late Cenozoic	Rift sediments	Sand along the lake or swamps more inland.
360–201 Ma	Karoo		Black shales, tillite, not metamorphosed.
1000–540 Ma	Neoproterozoic	Itombwe	Black shales, tillite, silicified tillite, weakly methamorphosed.
		Malagarasi	Black shales, tillite, silicified tillite, weakly methamorphosed. Presence of dolomites and volcanic rocks (basalts).
820–720 Ma		Alcaline complexes	Granitic rocks, intrusive volcanic rocks (rhyolite).
1375–980 Ma	Mesoproterozoic	Granites	two-mica and leucogranites.
1600–1000 Ma		Kivu	Pelites, quartzopelites, and quartzites at different degrees of weathering. Moderately metamorphosed.
2500–1600 Ma	Paleoproterozoic	Ruzizi and ante-Ruzizi	Gneiss and micaschists, prone to chemical weathering, and quartzites, resistant to weathering. Strongly methamorphosed.
4000–2500 Ma	Archaen		Gneiss and micaschists, prone to chemical weathering, and quartzites, resistant to weathering.

Table 1. Lithostratigraphical units in the NTK Rift, as presented by (Depicker et al., 2020), and based on the work of Laghmouch et al. (2018).

2.1.4 Rock strength and threshold slopes

In order to account for the control of lithology on the hillslope response to uplift and incision (Schmidt and Montgomery, 1995; Korup, 2008; Korup and Weidinger, 2011; Bennett et al., 2016), we classify the 12 lithostratigraphical units present in the NTK Rift (**Fig. 2d** and **Table 1**) into major categories based upon the analysis of their threshold slope, a proxy for rock strength
110 (Korup and Weidinger, 2011). We determine this value by analyzing the dependency of the average hillslope gradient, S, on the normalized steepness index, k_{sn}, averaged on a catchment scale (DiBiase et al., 2010; Bennett et al., 2016). We analyze first order catchments, whereby a drainage network was derived from the 1 arc second SRTM DEM data and a threshold catchment area of 10^5 m^2. For each lithostratigraphical unit, we only consider watersheds where more than 50 % of the area is covered with the dedicated lithostratigraphy.

115   The k_{sn} of a river segment is a proxy for the river incision rate and is calculated using the following equation (Wobus et al., 2006):

$$k_{sn} = S_{chan} A^{\theta_{ref}}, \tag{1}$$

with S_{chan} the local channel slope, A the upstream catchment area, and θ_{ref} the reference concavity index, set at 0.45 (See e.g. DiBiase and Whipple, 2011).

120   Theory suggests a positive linear relationship between S and k_{sn} in catchments with relatively low river incision rates. For catchments with high river incision rates, an increase in k_{sn} will not lead to further hillslope steepening, but to slope failure (DiBiase et al., 2010; Korup and Weidinger, 2011; Larsen and Montgomery, 2012), so that the S becomes independent of the k_{sn}. To capture this non-linear dependency of average basin slope on channel steepness, we introduce a new empirical relationship to describe the response of S to k_{sn}:

$$S = TA \left(1 - \exp\left(-\frac{a}{TA} k_{sn} \right) \right), \tag{2}$$

where parameter a is the slope of the curve at $k_{sn} = 0$. Thus, for low incision rates, a approximates the slope of the linear relationship between S and k_{sn}. Parameter TA is the slope angle to which the terrain converges for high k_{sn} values. Hence, TA can be considered equivalent to the threshold slope. However, when there is a linear relationship for $S = f(k_{sn})$ in the entire k_{sn} range, we do not consider the threshold estimate reliable.
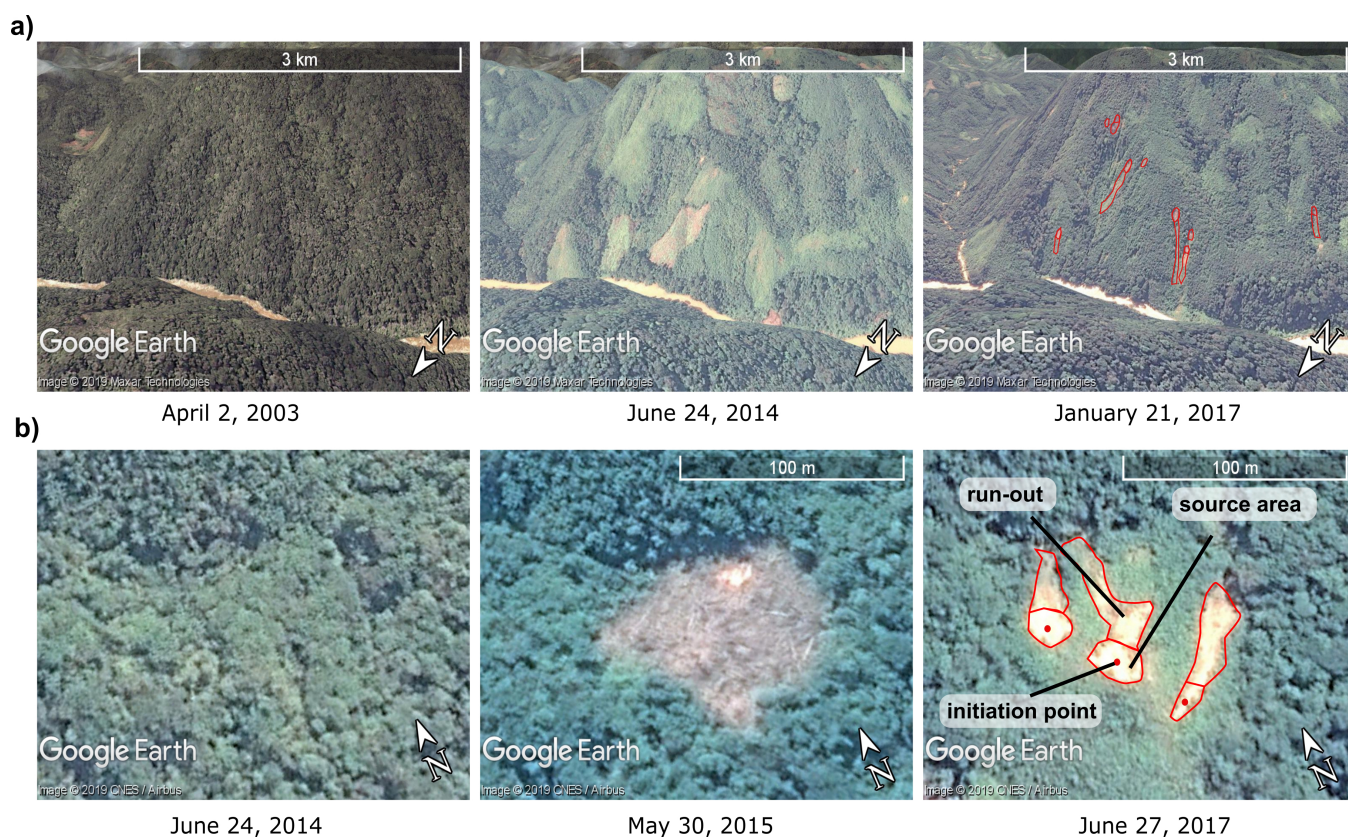
a)

b)

Figure 4. Examples of deforestation followed by landsliding. a) Landslide event North of Butezi, DRC (28.296984° E, 2.843201° S; image ©2019 Google Earth). **b)** Landslide event in Matale, DRC (28.360656° E, 2.645874° S; image ©2019 Google Earth).

2.2 Quantifying shallow landslide erosion

2.2.1 Inventory

The assessment of the shallow landslide erosion is based on a © Google Earth landslide inventory which is an update from
the dataset presented by Depicker et al. (2020). Only recent landslides, for which we can estimate the time of occurrence, are
considered in our inventory. In other words, the moment of failure must be situated between the timing of two images. Thus,
landslides that are detected in the oldest image of an imagery sequence are not incorporated in the database. Since we only
consider shallow landsliding in this study, we estimate the relative depth of the landslides (shallow or deep-seated) through *in
situ* field observations and/or by visually analyzing the shape and size of the landslide scarp and deposits in © Google Earth
imagery (Depicker et al., 2020). Each landslide is manually assigned a polygon delineating the source area to calculate the total
source area LS_S (m^2 km^{-2} year^{-1}). The LS_S is the area over which regolith material has been removed by landsliding and
serves as a proxy for landslide erosion. To each landslide, we also assign a point of initiation used to calculate the landslide
frequency LS_F (#LS km^{-2} year^{-1}). In order to calculate the LS_F as accurately as possible and avoid amalgamation, we
differentiate between separate source areas (Li et al., 2014; Marc et al., 2015; Roback et al., 2018).

Apart from amalgamation, our inventory can be biased due to the temporal and spatial inconsistency of © Google Earth.
The longer the observed time range, defined as the age difference between the oldest and youngest image, the more landslides
that are expected to have occurred. Similarly, we expect the landslide inventory to be less complete in areas of lower imagery
density (being the total number of images), as vegetation regrowth might erase the spectral signature of landslides before they
are captured in imagery. In order to quantify the imagery range and density, we manually identify all imagery footprints in ©
Google Earth. All images used in the analysis are of very-high spatial resolution, ranging from 30 to 60 cm. Areas with no
available imagery range or density are excluded from the analysis. We also pay attention to not inventory landslides linked to
mining and quarrying.

We investigate the impact of rejuvenation and forest cover on the size of the individual landslides in our inventory. The
one-sided Mann-Whitney U test is applied to statistically quantify any differences between different landslide populations
(McDonald, 2014).

2.2.2 Calculating landslide erosion rates from a biased © Google Earth inventory

In areas with no spatial or temporal bias in the available imagery, i.e. the imagery range and density are constant, the LS_F is
calculated as:

$$LS_F = \frac{n}{r\,A} \tag{3}$$

with n the total number of shallow landslides, A the total area covered by imagery, and r the imagery time range that is equal
for all observed landslides. However, © Google Earth imagery is biased and r has no constant value throughout the entire study
area. Hence we have to subdivide our study area in subareas j of equal time range r^j. The landslide frequency in each subarea

LS_F^j is then:

$$LS_F^j = \frac{n^j}{r^j \, A^j},\tag{4}$$

with n^j the number of landslides in subarea j, A^j the surface area of j, and r^j the constant time range in j. To calculate the frequency for the entire study area, the frequencies LS_F^j are averaged out using weights proportional to their area A^j:

165

$$LS_F = \sum_{j=1}^{N} \frac{A^j}{A} \, LS_F^j,\tag{5}$$

with N the number of subareas j. Substituting **Eq. (4)**, **Eq. (5)** becomes:

$$LS_F = \sum_{j=1}^{N} \frac{n^j}{r^j \, A},\tag{6}$$

which is equivalent to:

$$LS_F = \frac{1}{A} \sum_{i=1}^{n} \frac{1}{r^i},\tag{7}$$

170 with r^i the time range observed in landslide i. To compensate for differences in imagery density, necessary when comparing regions of different imagery coverage, we assume that the probability of identifying landslides increases linearly with imagery density. The equation then becomes:

$$LS_F = \frac{1}{A} \sum_{i=1}^{n} \frac{1}{r^i \, d^i},\tag{8}$$

with d^i the imagery density observed in landslide i. Note that there can be a saturation of the information provided by the
175 imagery: when the imagery density is high, the availability of one extra image will have no to little effect on the observed number of landslides. We address the issues of linearity and saturation by assessing the dependency of landslide density (# landslides km^{-2}) on imagery density. If the assumption of linearity does not hold, we have to apply a non-linear transformation on the d^i values. If saturation is problematic to our inventory, we have set a maximum value for d^i.

Deriving the LS_S equations is analogous to deriving the ones for the LS_F. We only have to slightly modify **Eq. (7)** and
180 **Eq. (8)**:

$$LS_S = \frac{1}{A} \sum_{i=1}^{n} \frac{a_{src}^i}{r^i},\tag{9}$$

$$LS_S = \frac{1}{A} \sum_{i=1}^{n} \frac{a_{src}^i}{r^i \, d^i},\tag{10}$$

whereby a_{src}^i is the source area of landslide i. Note that the LS_S will be less accurate than the LS_F due to biases in the
185 delineation of the landslide source area. These biases are caused by the time lag between the landslide occurrence and the

landslide detection in © Google Earth, whereby part of the source area might already have recovered. To avoid biases linked to the interpretation of the source area, all landslides were delineated by the same person. In order to statistically verify a difference in landslide activity between regions (for example rejuvenated versus relict landscapes), we use the one-sided non-parametric Mann-Whitney U test to compare the different landslide activity measures in fifth order water catchments (calculated with

190 **Eq. (8)** and **Eq. (10)** to compensate for imagery density differences).

2.2.3 Impact of slope on landslide erosion

We reclassify the slope values between 0-50° into 10 classes of equal width. For each slope class, we apply **Eq. (8)** and **(10)** separately. The uncertainty on the LS_S and LS_F is assessed by dividing the study area in 50 East-West bands of equal width. Subsequently, we calculate the LS_S and LS_F 50 times, each time leaving the data for one band out of the analysis. In other

195 words, for each run we slightly perturbate the landslide inventory. As such, we can assess the degree to which our LS_S and LS_F calculations are affected by outliers and/or extreme landslide events.

2.2.4 Linking forest cover and deforestation to landslide erosion

In order link forest dynamics to landslide erosion, we must distinguish between landslides that followed deforestation (**Fig. 4**) and landslides that caused deforestation. To identify the correct causality, we reconstructed the timeline of every landslide that

200 occurred on deforested land (**Fig. 5b**). Landslides following deforestation are defined as those that happened within the post-deforestation time range, being the period between the first image after the year of deforestation and the most recent image.

Determining the LS_S in function of the time elapsed since deforestation (t_{def}) is necessary to characterize the post-deforestation landslide wave. Yet, this analysis is far from straightforward (as t_{def} is temporally dynamic) and requires two

205 components: i) the total affected area of landslides that happened t_{def} years after deforestation, and ii) the total area $A_{t_{def}}$ in which we can observe land that was deforested t_{def} years ago. For the first component, we only include landslides for which the time between deforestation and landsliding ($t_{def \to LS}$) is equal to t_{def}. However, there is a considerable degree of uncertainty associated to $t_{def \to LS}$. Firstly, for each landslide, the exact moment of failure must be assumed to be distributed uniformly between the capture times of the image where it was initially observed and the preceding image. Secondly, we know the year

210 of deforestation but not the exact date. Here, we assume the deforestation time to be uniformly distributed in the reported year. To visualize these uncertainties, we recalculate the $t_{def \to LS}$ 100 times for each landslide, each time randomly sampling the moments of deforestation and landsliding. The second component, $A_{t_{def}}$, entails all areas where the sum of t_{def} and the year of deforestation lies in the range between the oldest and newest post-deforestation image in © Google Earth.
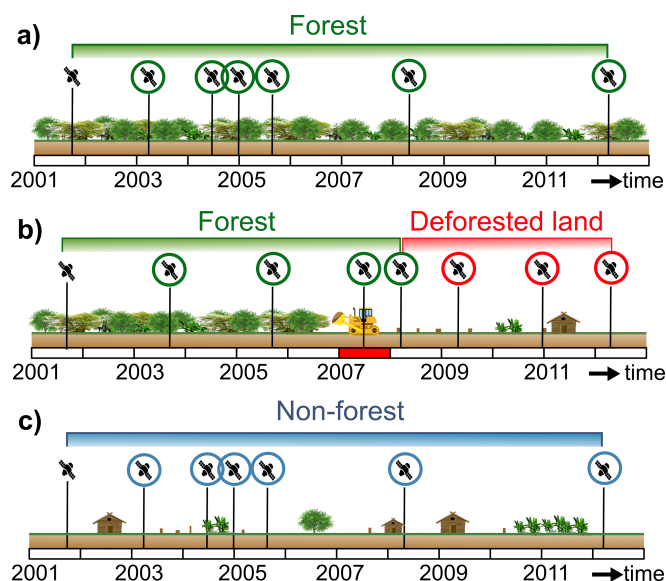
Figure 5. Schematic overview of the three considered forest cover scenarios in © Google Earth. The satellite icons signal the availability of a © Google Earth image and the colored circles indicate whether we can observe recent landslides in the concerned image. **a)** Forest scenario: each landslide observed in these areas is linked to forest cover. **b)** Deforestation scenario: only landslides observed in the second © Google Earth image after the year of deforestation are considered to be linked to deforestation (in other words, we can only observe deforestation-induced landslides in imagery that is encircled in red on the figure). The red bar indicates the year of deforestation. **c)** Non-forest scenario: every landslide observed in these regions is linked to non-forest.

3   Results

3.1   Regional controls on landslide erosion

We identified 834 knickpoints using a tolerance value of 100 m. From these, 673 knickpoints were considered non-stationary and were used to demarcate the rejuvenated Rift (**Fig. 6**). The rejuvenated landscapes encompass 15,526 km^2, or 18 % of the entire study area.

The average annual rainfall in the rejuvenated landscapes is significantly lower than in the relict landscapes (1,905 mm/year versus 2,297 mm/year, $p<0.01$). Similarly, we find that within the rejuvenated landscapes the 2 day 15 mm threshold is exceeded significantly less often compared to the relict landscapes ($p<0.01$), indicating that landslide-triggering rainfall events occur less frequently.

Based on the analysis of 234,840 first-order catchments, we identify three major lithological categories (**Fig. 7**). Category I comprises units that do not display clear threshold angles. These are lithostratigraphies of relatively young age such as recent and young volcanic basalts and lake and river sediments (all <23 Ma) except for the Malagarasi rock formations. The latter formation is of old age (1000-540 Ma) and covers only a small area in the Southeast of the study area. The lack of threshold
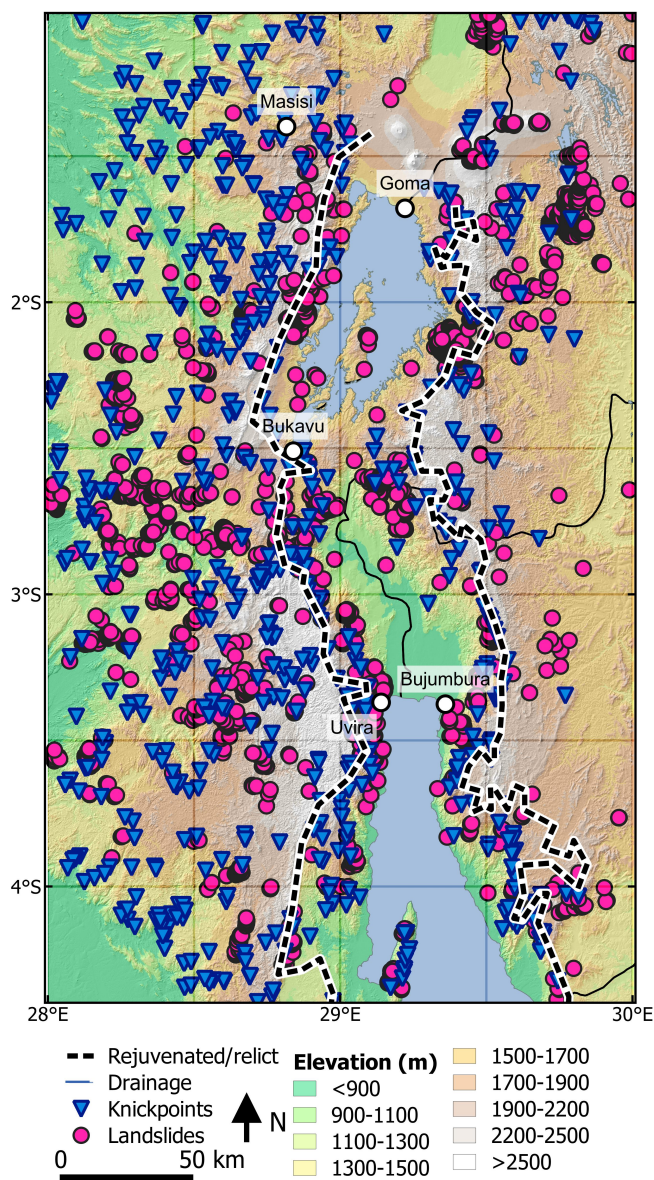
Figure 6. Landslide and knickpoint inventory for the NTK Rift. We identified 7994 shallow recent landslides and 834 knickpoints, of which 673 were considered non-stationary. These knickpoint were used to separate the rejuvenated landscapes between the Rift shoulders from the surrounding relict landscapes.
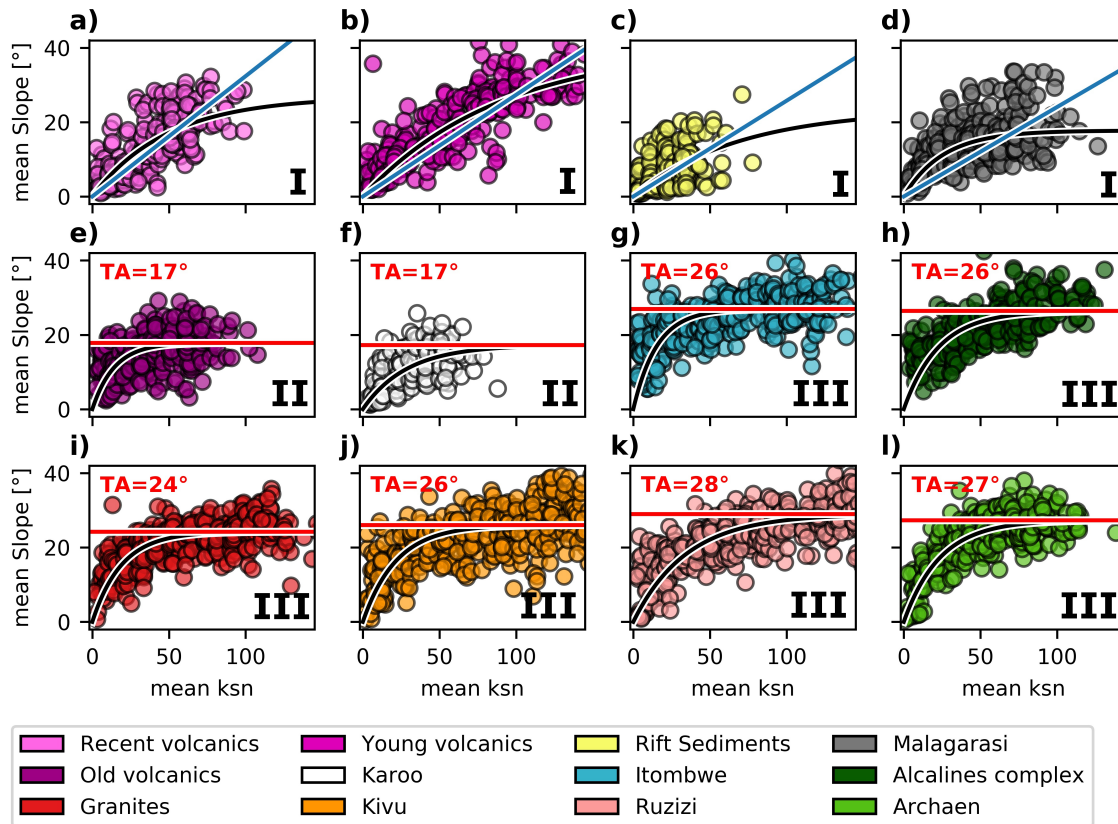
Figure 7. Threshold slope analysis for the different lithostratigraphical units in the NTK Rift. Based on the trends of the landscape slope gradient S versus the normalized river steepness index k_{sn} (the $S = f(k_{sn})$ relationship is presented by the black curve on each subplot; **Eq.** (2)), both averaged over first order river catchments. **a)→d)** Category I Young lithostratigraphy for which no clear threshold angle is observed. **e)→f)** Category II Young lithostratigraphy with a low threshold angle of ca. 17°. **g)→l)** Category III Older rocks with higher observed threshold slopes of 24-28°.

landscapes in Category I could be related to the fact that the duration of exposure to weathering for these rocks has been too short. Category II, consisting of old volcanic basalts and Karoo lithostratigraphy (both younger than 210 Ma) has threshold slopes of roughly 17°. Rocks of Category III, with observed threshold slopes ranging between 24-28°, are generally of older age (>540 Ma) and display a high resistance to slope failure. The lithostratigraphy of Category III includes the following formations: Itombwe, Alcaline complexes, Granites, Kivu, Ruzizi, and Archaen.

3.2 Shallow landslide erosion in the NTK Rift: impacts of deforestation and rejuvenation

We inventoried 7,944 recent shallow landslides (**Fig. 6**). Following the classification of Hungr et al. (2014), the observed landslides were mostly debris slides (often evolving into avalanches), debris/mud flows, and flowslides. Rocks of Category I

235 and II combined contained only 344 instances, hampering a robust analysis. We therefore focus our further analysis on the 7600 landslides in areas with rocks of Category III.

A total of 932 © Google Earth images, dating between 2000 and 2019, were identified. There is a great spatial variety in imagery range and density (**Fig. 8a-b**). The highest imagery density is available for the major cities in the study area (Goma, Bukavu, and Bujumbura), whereas the northwest and southwest regions have fewer observations. The number of observed

240 landslides increases linearly with the available imagery up to a density of 12 images (**Fig. 8c**). At more than 12 images, the imagery density is 'saturated': additional images offer no added-value for landslide detection. In our inventory, nearly 99 % of landslides occur in areas with imagery density ≤12 images. Hence, the assumption that landslide density is linearly dependent on imagery density is not violated within our study area and we take no measures to correct for saturation. The annual extent of imagery made available in © Google Earth increases with time, especially after 2010 (**Fig. 8d**).

245 After accounting for differences in imagery density, the overall LS_S in rejuvenated landscapes is roughly 40 % higher than in relict landscapes (p=0.034, **Fig. 9a**). The difference becomes even larger when looking at the LS_F (160 %, p=0.014, **Fig. 9b**), which implies that landslides are on average smaller in rejuvenated landscapes. This difference in landslide size between rejuvenated and relict landscapes is confirmed in all three land cover types: forests (114 versus 308 m^2, p<0.01), non-forests (111 versus 138 m^2, p<0.01), and deforested land (94 versus 239 m^2, p<0.01). Similar to the rejuvenation status, forest cover

250 also influences the landslide size. The average source area for forests (223 m^2) decreases non-significantly after deforestation (165 m^2, p =0.06). In non-forest lands, the landslide size (126 m^2) is significantly smaller than in recently deforested lands (p <0.01).

The LS_S and LS_F increase with slope gradient (**Fig. 10a-b,d-e**). A decrease is observed for forested slopes >45°, which could be linked to limitations on regolith formation, whereby weathering and sediment deposition are outpaced by erosion

255 (Montgomery, 2001). When comparing slopes of equal steepness, we observe that the LS_S is generally higher in relict landscapes than in rejuvenated landscapes (**Fig. 10c**). Nevertheless, the overall LS_S is higher in rejuvenated landscapes, because the overall predominance of steeper relief (**Fig. 10g-h**) compensates for the fact that, comparing similarly angled individual slopes in rejuvenated and relict zones, rejuvenated slopes are shown to have a lower or equal rate of shallow landslide erosion (**Fig. 10c**).

260 Recently deforested slopes are up to eight times more sensitive to shallow landsliding compared to forested slopes (**Fig. 10a-b**). The deforestation effect lasts approximately 15 years (**Fig. 11**). However, deforestation increases LS_S much more in relict landscapes compared to rejuvenated areas (**Fig. 10c**). The LS_S in the 'non-forested' areas (blue lines in **Fig. 10**) corresponds to the situation that prevails once the deforestation-induced landslide wave has passed. In this situation, the LS_S drops back to a level similar to that observed under forest (green line) (**Fig. 10a-b**).
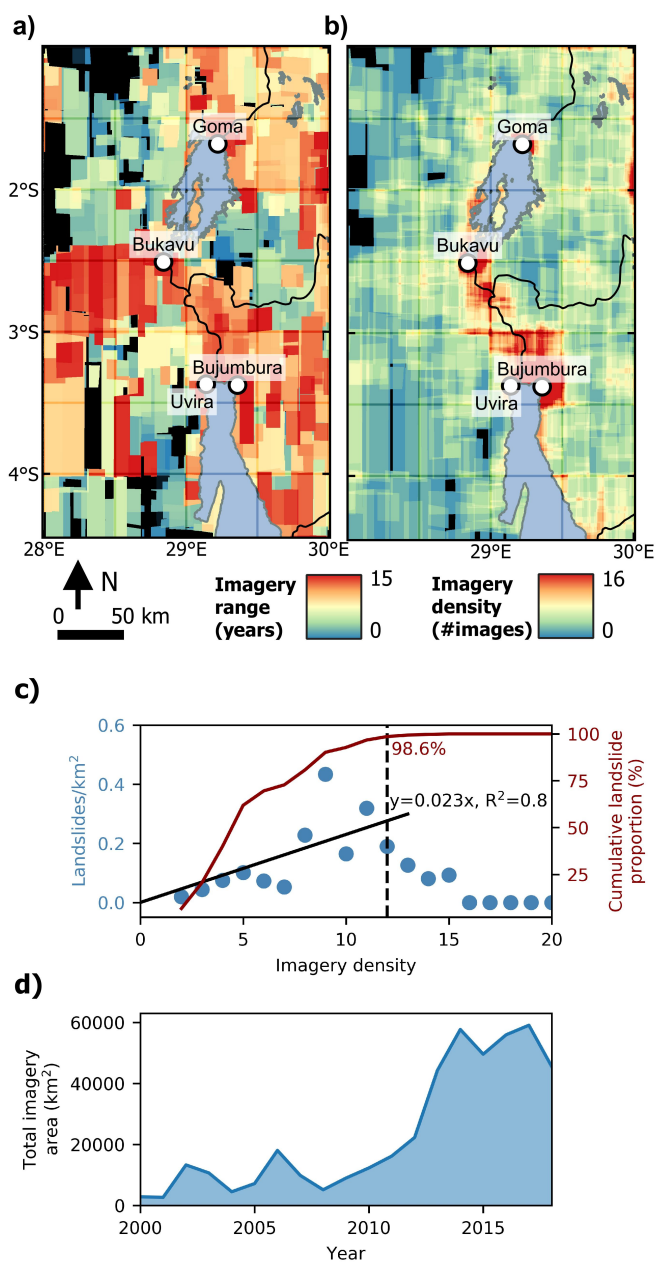
Figure 8. Visualization of the imagery bias in © Google Earth. a) Imagery range. **b)** Imagery density. **c)** Impact of the imagery density on the number of observed landslides. **d)** The evolution of imagery availability between 2000 and 2018.
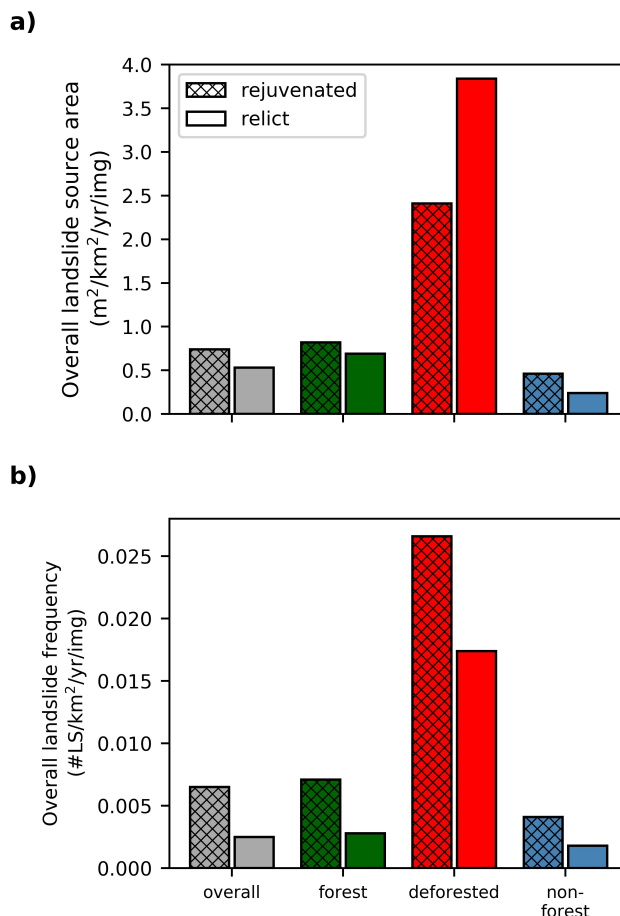
Figure 9. Overall landslide activity in the NTK Rift, adjusted for imagery density. **a)** Overall landslide source area (LS_S), a proxy for landslide erosion. **b)** Landslide frequency (LS_F).

4 Discussion

4.1 Interactions between deforestation, rejuvenation, and landslide erosion

We found that steep ($>35°$) forested slopes of equal steepness display higher shallow landslide erosion rates (approximated by the LS_S) in relict landscapes than in rejuvenated landscapes (**Fig. 10c**). A first explanation for this difference could be the drier climate in the rejuvenated landscapes. Based on the global rainfall threshold proposed by Guzzetti et al. (2008), it is likely that landslide-triggering rainfall events are on average more frequent in relict areas compared to rejuvenated landscapes. However, it should be noted that the difference in landslide erosion rates between rejuvenated and relict landscapes under forest is not due to a higher frequency of landsliding events in relict areas. On the contrary, LS_F is much higher in rejuvenated landscapes (**Fig. 10f**). If rainfall explains the difference in erosion between rejuvenated and relict landscapes, this could be due

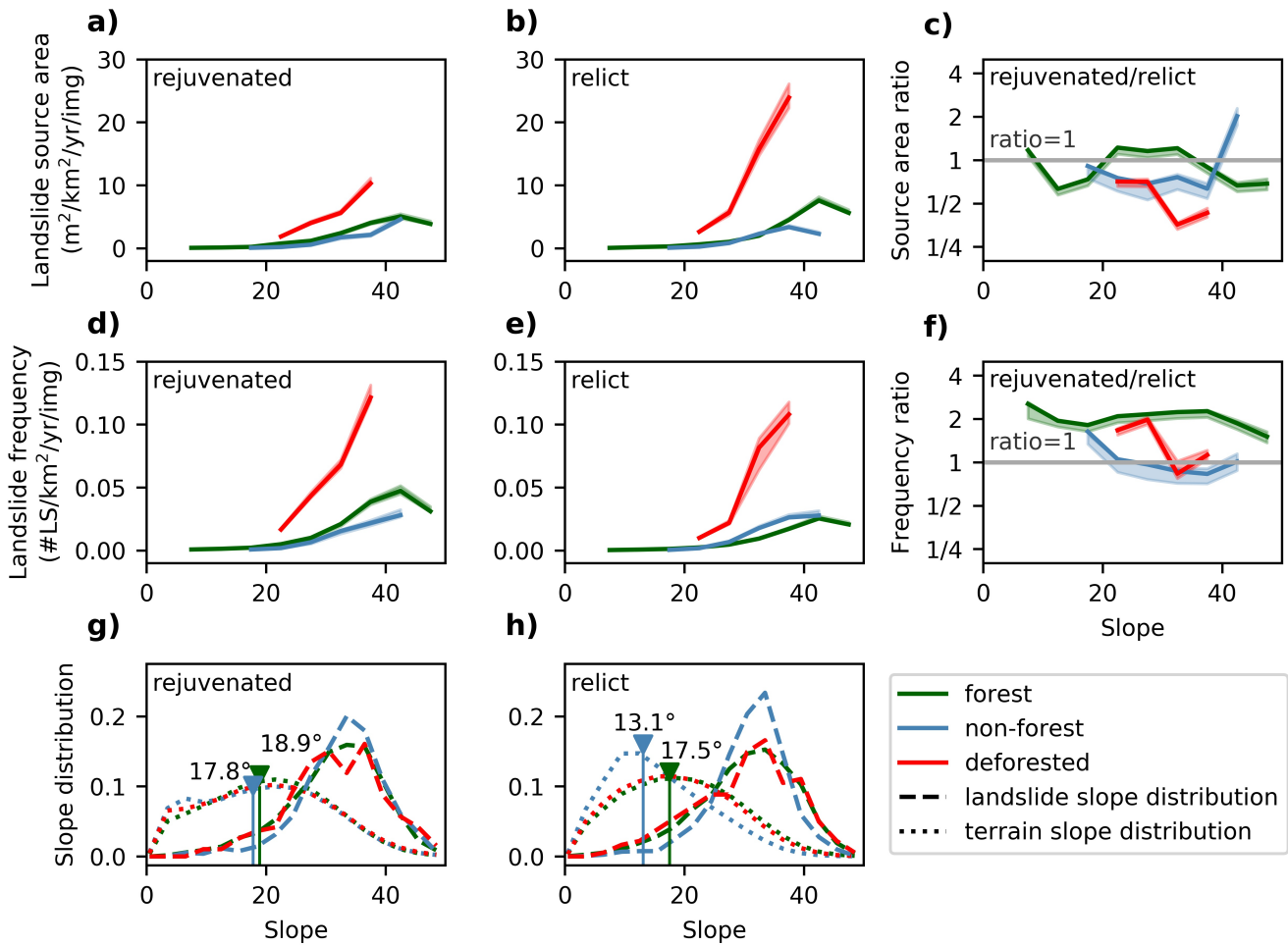Earth **Surface**
Dynamics
Discussions

EGU

Figure 10. The effect of slope steepness and rejuvenation on landslide activity, corrected for imagery density. We only show results for slope classes in which we observed more than 20 landslides. **a)→c)** Landslide source area (LS_S) in function of slope. **d)→f)** Landslide frequency (LS_F) in function of slope. **g)→h)** Slope distribution for the terrain and landslides in the rejuvenated and relict landscapes. The blue and green arrows indicate the median slope in non-forest and forest landscapes. The slopes in rejuvenated landscapes are clearly steeper, both in forest and non-forest land.

to the triggering of larger, rather than more, landslides. However, disentangling the relationship between rainfall and landslide

275   frequency/erosion is complicated by the influence of other regional controls, such as seismicity and regolith availability.

     A second factor that needs to be considered when evaluating differences in landslide erosion is the difference in seismic activity between the rejuvenated and relict landscapes (Delvaux and Barth, 2010). We hypothesize that the higher seismic activity in rejuvenated landscapes would result in elevated landslide erosion rates on longer timescales due to the occurrence of major landslide events triggered by large earthquakes (Marc et al., 2015). However, in our observed period, no landslide-
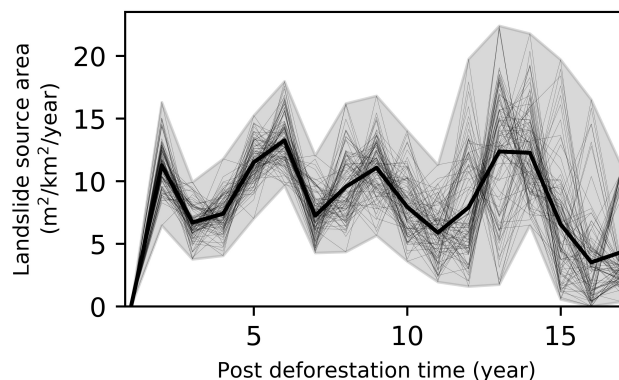
Earth **Surface**
Dynamics
Discussions

Figure 11. Deforestation-induced landslide wave. Overall landslide source area (LS_S, m^2 km^{-2} year^{-1}) in function of time elapsed since deforestation. There are not enough observations to make two separate consistent plots for rejuvenated and relict landscapes (**Fig. A1**)

280   triggering earthquakes occurred (Dewitte et al., 2020). The absence of such events suggests that our window of observation is too short to capture the direct impact of large earthquakes on landslide erosion within the rejuvenated NTK Rift. Over the long term, the contribution of earthquake-induced landsliding to regolith mobilization may nevertheless be important. Weak seismic activity also contributes to the smaller size and higher frequency of observed landslides in the rejuvenated part of the study area; earthquakes fracture and weaken the bedrock and hence reduce the minimum critical area for landslide initiation

285   (Delvaux and Barth, 2010; Milledge et al., 2014; Vanmaercke et al., 2017)

     A third factor potentially contributing to the difference in erosion on equal slopes (**Fig. 10c**) is that the regolith cover on rejuvenated slopes is expected to be thinner and less continuous due to the drier climate, the younger age of the landscape, the continuous adaptation to river incision, and sporadic earthquake-triggered landslide events (Schoenbohm et al., 2004; Egholm et al., 2013; Marc et al., 2015; Braun et al., 2016), thereby inducing a supply-limited landsliding regime. This can

290   also partly explain why the rejuvenated landscapes have more, but smaller landslides in comparison to relict landscapes, as the size of the shallow landslides is constraint by the regolith availability. However, we do not have direct evidence supporting this hypothesis: The collection of field data on regolith thickness is hampered by limited access to the field, especially in the eastern DRC. Alternatively, regolith depth could be derived from landslide scars observed on a high-resolution DEM, but such product is currently not available.

295   We find that the landslide response to deforestation is much more pronounced in relict landscapes than in rejuvenated landscapes (**Fig. 10c**). This observation may also be linked to the drier climate and seismic fracturing in the rejuvenated landscape, as we observe more but smaller landslides (**Fig. 10c and 10f**). Differences in regolith availability can also be invoked to explain the different response of these landscapes to deforestation. Assuming that rejuvenated areas are indeed devoid of regolith (in comparison to relict areas), one may expect that deforestation will lead to a less important response

300   in rejuvenated areas, simply because the stock of material that can be mobilized through landsliding is smaller. Overall, the deforestation wave persists over a time-scale of about 15 years (**Fig. 11**), which is consistent with reports in other studies

(e.g. Sidle and Bogaard, 2016). After the wave has passed, landslide erosion rates decrease to a level similar to that of forest conditions.

The erosion rates in non-forest land are much lower than in deforested areas and, in fact, similar to or lower than what
305 has been observed in forests (**Fig. 10a-b**). Thus, the fading-out of the deforestation-induced landslide wave in non-forest land cannot be explained by the recovery of forest vegetation. Moreover, the results imply that soils are protected as efficiently by forest cover as by grassland and crops, despite the presence of human practices such as terracing that could promote landsliding (Sidle and Ochiai, 2006). However, this is extremely unlikely given the much smaller rooting depths of both grasses and crops (Holdo et al., 2018). A more probable explanation for the fading-out of the deforestation-induced landslide wave is therefore
310 that landslide frequency and erosion rate return to lower levels once the most landslide-sensitive regolith has been removed. For those slopes that are stripped of their regolith cover after deforestation, the rainfall threshold for slope failure is temporarily increased and it may take thousands of years to redevelop a regolith depth that matches the pre-failure conditions (Hufschmidt and Crozier, 2008; Parker et al., 2016). Additionally, depending on the properties of the landslide deposits (e.g. fine-grained or rock debris), slopes might also experience depositional hardening due to an increase in bulk density and cohesion of the slope
315 material (Crozier and Preston, 1999; Brooks et al., 2002), yet field data is required to test this hypothesis.

Despite the fact that equal slopes in non-forest and forest land display similar landslide erosion rates, the average source area is significantly smaller in non-forest landscapes. The smaller size is likely due to a smaller minimum critical landslide area linked to the absence of tree cover (Milledge et al., 2014; Sidle and Bogaard, 2016). Hence, landslides in non-forest and forest land have different size characteristics, but the total erosion rate in function of slope remains similar.

320 **4.2 A new approach for calculating landslides erosion rates?**

Using **Eq.** (9) which deals with the biases in the © Google Earth imagery range, we obtain an overall LS_S of 4.86 m^2 km^{-2} year^{-1} in rejuvenated landscapes. Adopting an estimated average landslide depth of 2.5 m, this figure corresponds to a denudation rate of 0.012 mm year^{-1}. It can be compared to the regional uplift rates to estimate the importance of shallow landsliding in the overall evolution of the NTK Rift. There are no accurate estimates of the uplift rates in the study area,
325 but the maximal estimation in the Rwenzori Mountains, a particularly tectonically active region located 150 km North of our study area, is 2 mm year^{-1} (Kaufmann et al., 2016). If we consider similar rates in the NTK Rift, shallow landslide erosion compensates merely 0.6 % of the uplift in the rejuvenated landscapes, assuming a steady state between uplift and denudation. If we assume a much more conservative value of 0.2 mm year^{-1} (Montgomery and Brandon, 2002, e.g.), shallow landslide erosion compensates 6.1 % of the uplift rate. Both the upper and lower estimation suggest that, while shallow landslides are
330 highly visible in the landscapes we studied, their geomorphic effect is somewhat limited. In addition , it must be noted that the estimated erosion rate due to shallow landsliding is most likely an underestimation. First, we did not observe earthquake-induced landslide events, which are rare but may lead to catastrophic landslide erosion (Marc et al., 2015; Dewitte et al., 2020). Second, the landslide inventory used to calculate the erosion rate is incomplete due to limitations in © Google Earth coverage. Furthermore, we focused on shallow landsliding but other erosion processes such as deep-seated landsliding may
335 also contribute significantly to sediment mobilization (Dewitte et al., 2020; Depicker et al., 2020). Nevertheless, it is to be

expected that overall erosion rates are lower than uplift rates: this is the basic explanation as to why mountainous topography is formed.

5   Conclusions

We studied shallow landsliding along the NTK rift in order to understand how the interplay of landscape rejuvenation and
340 deforestation affects landslide erosion rates. Rejuvenated landscapes display a higher shallow landslide erosion rate than relict landscapes. This difference is due to the generally steeper relief in rejuvenated landscapes which more than compensates for the fact that rejuvenated slopes, when compared to similarly angled slopes in relict zones, often display a somewhat lower landslide erosion rate. These lower rates in the rejuvenated landscapes could be the result of a drier climate, the omission of earthquake-induced landslide events in our inventory, and potentially a smaller regolith stock. The latter hypothesis is consistent
345 with our observations that deforestation initiates a much larger landslide peak in relict landscapes and that landslides are, on average, much smaller in rejuvenated landscapes. Thus, the response of a landscape to deforestation does not only depend on local topography and climate but also on the geomorphic status of the landscape. Understanding this differential response is also important to assess the risk for the local population. Our study shows that such understanding is only possible if (i) inventory biases linked to © Google Earth imagery are properly eliminated, (ii) landscape status (rejuvenated versus relict) is
350 accounted for, and (iii) a sufficiently long time frame is considered to capture the transient nature of the deforestation-induced landslide wave.

Earth **Surface**
Dynamics
Discussions
Open Access
EGU

Earth Surface
Dynamics
Discussions

References

Aleman, J. C., Jarzyna, M. A., and Staver, A. C.: Forest extent and deforestation in tropical Africa since 1900, Nature Ecology and Evolution, 2, 26–33, https://doi.org/10.1038/s41559-017-0406-1, http://dx.doi.org/10.1038/s41559-017-0406-1, 2018.

Baynes, E. R., Lague, D., Attal, M., Gangloff, A., Kirstein, L. A., and Dugmore, A. J.: River self-organisation inhibits discharge control on
370   waterfall migration, Scientific Reports, 8, 1–8, https://doi.org/10.1038/s41598-018-20767-6, 2018.

Bennett, G. L., Miller, S. R., Roering, J. J., and Schmidt, D. A.: Landslides, threshold slopes, and the survival of relict terrain in the wake of the Mendocino Triple Junction, Geology, 44, 363–366, https://doi.org/10.1130/G37530.1, 2016.

Braun, J., Mercier, J., Guillocheau, F., and Robin, C.: A simple model for regolith formation by chemical weathering, Journal of Geophysical Research: Earth Surface, 121, 2140–2171, https://doi.org/10.1002/2016JF003914, 2016.

375 Brooks, S. M., Crozier, M. J., Preston, N. J., and Anderson, M. G.: Regolith stripping and the control of shallow translational hillslope failure: Application of a two-dimensional coupled soil hydrology-slope stability model, Hawke's Bay, New Zealand, Geomorphology, 45, 165–179, https://doi.org/10.1016/S0169-555X(01)00153-2, 2002.

Burbank, D. W., Leland, J., Fielding, E., Anderson, R. S., Brozovic, N., Reid, M. R., and Duncan, C.: Bedrock incision, rock uplift and threshold hillslopes in the northwestern Himalayas, Nature, 379, 505–510, https://doi.org/10.1038/379505a0, 1996.

380 Campforts, B., Vanacker, V., Herman, F., Vanmaercke, M., Schwanghart, W., Tenorio, G. E., Willems, P., and Govers, G.: Parameterization of river incision models requires accounting for environmental heterogeneity: insights from the tropical Andes, Earth Surface Dynamics, 8, 447–470, https://doi.org/10.5194/esurf-8-447-2020, https://www.earth-surf-dynam.net/8/447/2020/, 2020.

Crozier, M. J.: Deciphering the effect of climate change on landslide activity: a review, Geomorphology, 124, 260–267, https://doi.org/10.1016/j.geomorph.2009.09.010, 2010.

385 Crozier, M. J. and Preston, N. J.: Modelling Changes in Terrain Resistance as a Component of Landform Evolution in Unstable Hill Country, in: Process Modelling and Landform Evolution. Lecture Notes in Earth Sciences, vol. 78, edited by Hergarten, S. and Neugebauer, H. J., pp. 267–284, Springer-Verlag Berlin Heidelberg, 1999.

Delvaux, D. and Barth, A.: African stress pattern from formal inversion of focal mechanism data, Tectonophysics, 482, 105–128, https://doi.org/10.1016/j.tecto.2009.05.009, 2010.

390 Delvaux, D., Mulumba, J.-L., Sebagenzi, M. N. S., Bondo, S. F., Kervyn, F., and Havenith, H.-B.: Seismic hazard assessment of the Kivu rift segment based on a new seismotectonic zonation model (western branch, East African Rift system), Journal of African Earth Sciences, 134, 831–855, https://doi.org/10.1016/j.jafrearsci.2016.10.004, 2017.

Depicker, A., Jacobs, L., Delvaux, D., Havenith, H.-B., Maki Mateso, J.-C., Govers, G., and Dewitte, O.: The added value of a regional landslide susceptibility assessment: The western branch of the East African Rift, Geomorphology, 353, 106 886,
395   https://doi.org/10.1016/j.geomorph.2019.106886, 2020.

Dewitte, O., Dille, A., Depicker, A., Kubwimana, D., Maki-Mateso, J.-C., Mugaruka Bibentyo, T., Uwihirwe, J., and Monsieurs, E.: Constraining landslide timing in a data-scarce context: from recent to very old processes in the tropical environment of the North Tanganyika-Kivu Rift region, Landslides, https://doi.org/10.1007/s10346-020-01452-0, 2020.

DiBiase, R. A. and Whipple, K. X.: The influence of erosion thresholds and runoff variability on the relationships among topography, climate,
400   and erosion rate, Journal of Geophysical Research: Earth Surface, 116, 1–17, https://doi.org/10.1029/2011JF002095, 2011.

Earth Surface
Dynamics
Discussions

DiBiase, R. A., Whipple, K. X., Heimsath, A. M., and Ouimet, W. B.: Landscape form and millennial erosion rates in the San Gabriel Mountains, CA, Earth and Planetary Science Letters, 289, 134–144, https://doi.org/10.1016/j.epsl.2009.10.036, http://dx.doi.org/10.1016/j.epsl.2009.10.036, 2010.

Egholm, D. L., Knudsen, M. F., and Sandiford, M.: Lifespan of mountain ranges scaled by feedbacks between landsliding and erosion by rivers, Nature, 498, 475–478, https://doi.org/10.1038/nature12218, 2013.

Ellis, E. C., Goldewijk, K. K., Siebert, S., Lightman, D., and Ramankutty, N.: Anthropogenic transformation of the biomes, 1700 to 2000, Global Ecology and Biogeography, 19, 589–606, https://doi.org/10.1111/j.1466-8238.2010.00540.x, 2010.

Guzzetti, F., Peruccacci, S., Rossi, M., and Stark, C. P.: The rainfall intensity-duration control of shallow landslides and debris flows: An update, Landslides, 5, 3–17, https://doi.org/10.1007/s10346-007-0112-1, 2008.

Hansen, M. C., Potapov, P., Moore, R., Hancher, M., Turubanova, S., Tyukavina, A., Thau, D., Stehman, S., Goetz, S., Loveland, T., Kommareddy, A., Egorov, A., Chini, L., Justice, C., and Townshend, J.: High-Resolution Global Maps of 21st-Century Forest Cover Change, Science, 342, 850–853, https://doi.org/10.1126/science.1244693, 2013.

Holdo, R. M., Nippert, J. B., and Mack, M. C.: Rooting depth varies differentially in trees and grasses as a function of mean annual rainfall in an African savanna, Oecologia, 186, 269–280, https://doi.org/10.1007/s00442-017-4011-4, 2018.

Hufschmidt, G. and Crozier, M. J.: Evolution of natural risk: Analysing changing landslide hazard in Wellington, Aotearoa/New Zealand, Natural Hazards, 45, 255–276, https://doi.org/10.1007/s11069-007-9158-6, 2008.

Hungr, O., Lerouel, S., and Picarelli, L.: The Varnes classification of landslide types, an update, Landslides, 11, 167–194, https://doi.org/10.1007/s10346-013-0436-y, 2014.

JRC and CIESIN: GHS population grid, derived from GPW4, multitemporal (1975, 1990, 2000, 2015). Accessed August 12, 2020 (http://data.europa.eu/89h/jrc-ghsl-ghs_pop_gpw4_globe_r2015a), 2015.

Kaufmann, G., Hinderer, M., and Romanov, D.: Shaping the Rwenzoris: balancing uplift, erosion, and glaciation, International Journal of Earth Sciences, 105, 1761–1778, https://doi.org/10.1007/s00531-015-1174-2, http://dx.doi.org/10.1007/s00531-015-1174-2, 2016.

Kirby, E. and Whipple, K. X.: Expression of active tectonics in erosional landscapes, Journal of Structural Geology, 44, 54–75, https://doi.org/10.1016/j.jsg.2012.07.009, http://dx.doi.org/10.1016/j.jsg.2012.07.009, 2012.

Korup, O.: Rock type leaves topographic signature in landslide-dominated mountain ranges, Geophysical Research Letters, 35, 1–5, https://doi.org/10.1029/2008GL034157, 2008.

Korup, O. and Weidinger, J. T.: Rock type, precipitation, and the steepness of Himalayan threshold hillslopes, Geological Society, London, Special Publications, 353, 235–249, https://doi.org/10.1144/SP353.12, http://sp.lyellcollection.org/lookup/doi/10.1144/SP353.12, 2011.

Laghmouch, M., Kalikone, C., Ilombe, G., Ganza, G., Delvaux, D., Safari, E., Bachinyaga, J., Wazi, N., Nzolang, C., Fernandez, M., Nimpagaritse, G., Tack, L., Dewaele, S., and Kervyn, F.: Carte géologique du Kivu au 1/500 000, Africamuseum (Tervuren, Belgique), Université Officielle de Bukavu (Bukavu, DRC), 2018.

Larsen, I. J. and Montgomery, D. R.: Landslide erosion coupled to tectonics and river incision, Nature Geoscience, 5, 468–473, https://doi.org/10.1038/NGEO1479, 2012.

Li, G., West, A. J., Densmore, A. L., Jin, Z., Parker, R. N., and Hilton, R. G.: Seismic mountain building: landslides associated with the 2008 Wenchuan earthquake in the context of a generalized model for earthquake volume balance, Geochemistry, Geophysics, Geosystems, 15, 833–844, 2014.

Marc, O., Hovius, N., Meunier, P., Uchida, T., and Hayashi, S.: Transient changes of landslide rates after earthquakes, Geology, 43, 883–886, https://doi.org/10.1130/G36961.1, 2015.

Earth Surface
Dynamics
Discussions

McDonald, J.: Handbook of Biological Statistics, Sparky House Publishing, Baltimore, MD, 3rd edn., 2014.

440 Milledge, D. G., Bellugi, D., Mckean, J. A., Densmore, A. L., and Dietrich, W. E.: A multidimensional stability model for predicting shallow landslide size and shape across landscapes, Journal of Geophysical Research: Earth Surface, 119, 2481–2504, https://doi.org/10.1002/2014JF003135, 2014.

Monsieurs, E., Jacobs, L., Michellier, C., Basimike, J., Bamulezi Ganza, G., Kervyn, F., Maki Mateso, J.-C., Mugaruka Bibentyo., T., Kalikone Buzera, C., Nahimana, L., Ndayisenga, A., Nkurunziza, P., Thiery, W., Demoulin, A., Kervyn, M., and Dewitte, O.: Landslide
445 inventory for hazard assessment in a data- poor context: a regional-scale approach in a tropical African environment, Landslides, 15, 2195–2209, https://doi.org/10.1007/s10346-018-1008-y, 2018a.

Monsieurs, E., Kirschbaum, D. B., Tan, J., Maki Mateso, J. C., Jacobs, L., Plisnier, P. D., Thiery, W., Umutoni, A., Musoni, D., Bibentyo, T. M., Ganza, G. B., Mawe, G. I., Bagalwa, L., Kankurize, C., Michellier, C., Stanley, T., Kervyn, F., Kervyn, M., Demoulin, A., and Dewitte, O.: Evaluating TMPA rainfall over the sparsely gauged East African Rift, Journal of Hydrometeorology, 19, 1507–1528,
450 https://doi.org/10.1175/JHM-D-18-0103.1, 2018b.

Montgomery, D., Schmidt, K., Greenberg, H., and Dietrich, W.: Forest clearing and regional landsliding, Geology, 28, 311–314, https://doi.org/10.1130/0091-7613(2000)28<311:FCARL>2.0.CO;2, 2000.

Montgomery, D. R.: Slope distributions, threshold hillslopes, and steady-state topography, American Journal of Science, 301, 432–454, https://doi.org/10.2475/ajs.301.4-5.432, 2001.

455 Montgomery, D. R. and Brandon, M. T.: Topographic controls on erosion rates in tectonically active mountain ranges, Earth and Planetary Science Letters, 201, 481–489, https://doi.org/10.1016/S0012-821X(02)00725-2, 2002.

Mugagga, F., Kakembo, V., and Buyinza, M.: Land use changes on the slopes of Mount Elgon and the implications for the occurrence of landslides, Catena, 90, 39–46, https://doi.org/10.1016/j.catena.2011.11.004, http://dx.doi.org/10.1016/j.catena.2011.11.004, 2012.

Musumba Teso, P., Kavira, M., and Katcho, K.: Key Factors Driving Deforestation in North-Kivu Province, Eastern DR-Congo Using
460 GIS and Remote Sensing, American Journal of Geographic Information System, 8, 11–25, https://doi.org/10.5923/j.ajgis.20190801.02, http://article.sapub.org/10.5923.j.ajgis.20190801.02.html, 2019.

Parker, R. N., Hales, T. C., Mudd, S. M., Grieve, S. W. D., and Constantine, J. A.: Colluvium supply in humid regions limits the frequency of storm-triggered landslides, Scientific Reports, 6, 1, 2016.

Roback, K., Clark, M. K., West, A. J., Zekkos, D., Li, G., Gallen, S. F., Chamlagain, D., and Godt, J. W.: The size, dis-
465 tribution, and mobility of landslides caused by the 2015 Mw7.8 Gorkha earthquake, Nepal, Geomorphology, 301, 121–138, https://doi.org/10.1016/j.geomorph.2017.01.030, 2018.

Saria, E., Calais, E., Stamps, D. S., Delvaux, D., and Hartnady, C. J. H.: Present-day kinematics of the East African rift, Journal of Geophysical Research: Solid Earth, 119, 3584–3600, https://doi.org/DOI: 10.1002/2013JB010901, 2014.

Schmidt, K. M. and Montgomery, D. R.: Limits to Relief, Science, 270, 617–620, https://doi.org/10.1126/science.270.5236.617, 1995.

470 Schoenbohm, L. M., Whipple, K. X., Burchfiel, B. C., and Chen, L.: Geomorphic constraints on surface uplift, exhumation, and plateau growth in the Red River region, Yunnan Province, China, Geological Society of America Bulletin, 116, 895–909, https://doi.org/10.1130/B25364.1, 2004.

Schwanghart, W. and Scherler, D.: Bumps in river profiles: Uncertainty assessment and smoothing using quantile regression techniques, Earth Surface Dynamics, 5, 821–839, https://doi.org/10.5194/esurf-5-821-2017, 2017.

475 Sidle, R. C. and Bogaard, T. A.: Dynamic earth system and ecological controls of rainfall-initiated landslides, Earth-Science Reviews, 159, 275–291, https://doi.org/10.1016/j.earscirev.2016.05.013, 2016.

Sidle, R. C. and Ochiai, H.: Landslides: Processes, Prediction and Land Use, American geophysical union, https://doi.org/10.1029/WM018, 2006.

Sidle, R. C., Ziegler, A. D., Negishi, J. N., Nik, A. R., Siew, R., and Turkelboom, F.: Erosion processes in steep terrain—Truths, myths, and
480   uncertainties related to forest management in Southeast Asia, Forest Ecology and Management, 224, 199–225, 2006.

Smets, B., Kervyn, M., D'Oreye, N., and Kervyn, F.: Spatio-temporal dynamics of eruptions in a youthful extensional setting: Insights from Nyamulagira Volcano (D.R. Congo), in the western branch of the East African Rift, Earth-Science Reviews, 150, 305–328, https://doi.org/10.1016/j.earscirev.2015.08.008, http://dx.doi.org/10.1016/j.earscirev.2015.08.008, 2015.

Tyukavina, A., Hansen, M. C., Potapov, P., Parker, D., Okpa, C., Stehman, S. V., Kommareddy, I., and Turubanova, S.: Congo Basin forest
485   loss dominated by increasing smallholder clearing, Science Advances, 4, https://doi.org/10.1126/sciadv.aat2993, 2018.

USGS: Shuttle Radar Topography Mission, Global Land Cover Facility. 1 Arc-Second. University of Maryland, College Park, Maryland, 2006.

USGS: LANDSAT-8, ETM+SLC-on. 60 m resolution., 2018.

Van de Walle, J., Thiery, W., Brousse, O., Souverijns, N., Demuzere, M., and van Lipzig, N. P.: A convection-permitting model for the
490   Lake Victoria Basin: evaluation and insight into the mesoscale versus synoptic atmospheric dynamics, Climate Dynamics, 54, 1779–1799, https://doi.org/10.1007/s00382-019-05088-2, https://doi.org/10.1007/s00382-019-05088-2, 2019.

Vanmaercke, M., Ardizzone, A., Rossi, M., and Guzzetti, F.: Exploring the effects of seismicity on landslides and catchment sediment yield: An Italian case study, Geomorphology, 278, 171–183, https://doi.org/10.1016/j.geomorph.2016.11.010, 2017.

Wobus, C., Whipple, K. X., Kirby, E., Snyder, N., Johnson, J., Spyropolou, K., Crosby, B., and Sheehan, D.: Tectonics from topography:
495   Procedures, promise, and pitfalls, Special Paper of the Geological Society of America, 398, 55–74, https://doi.org/10.1130/2006.2398(04), 2006.

Appendix A: Deforestation wave in rejuvenated and relict landscapes

a) Rejuvenated
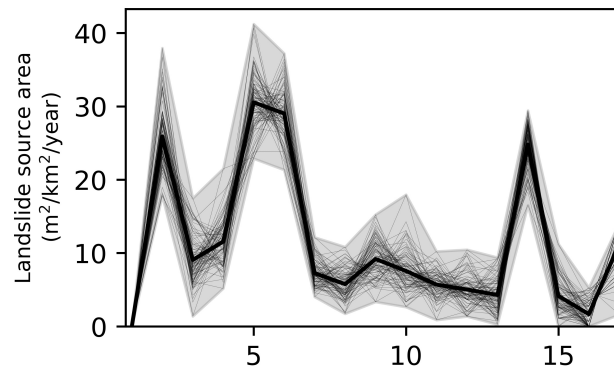
b) Relict

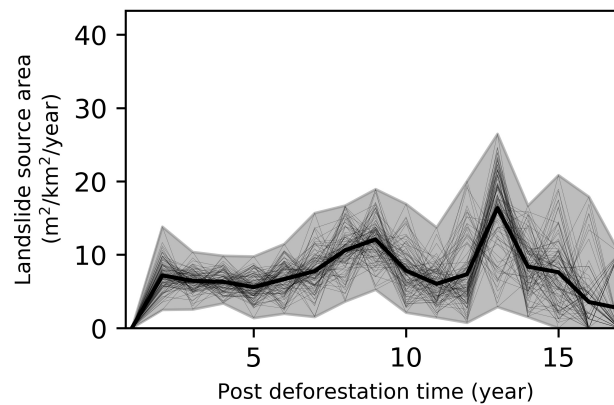**Figure A1. Deforestation-induced landslide wave in different geomorphic contexts. a)** Rejuvenated landscapes. The irregular curve suggests that we need more landslide observations to characterize the deforestation-induced landslide wave. **b)** Relict landscapes.